

Article

Nitrogen-Rich Triazine-Based Covalent Organic Frameworks as Efficient Visible Light Photocatalysts for Hydrogen Peroxide Production

Shu Yang^{1,2,†}, Keke Zhi^{3,4,†} , Zhimin Zhang^{1,2}, Rukiya Kerem^{1,2}, Qiong Hong^{1,2}, Lei Zhao^{1,2}, Wenbo Wu¹, Lulu Wang^{1,2,*} and Duozhi Wang^{1,2,*}

¹ College of Chemistry, Xinjiang University, Urumqi 830017, China; ys18536398768@sina.com (S.Y.); z18190914@sina.com (Z.Z.); rky_k223@sina.com (R.K.); hongqiong0809@sina.com (Q.H.); 14719415415m@sina.cn (L.Z.); ww100605249@sina.com (W.W.)

² State Key Laboratory of Chemistry and Utilization of Carbon Based Energy Resources, Urumqi 830017, China

³ College of Engineering, China University of Petroleum—Beijing at Karamay, Karamay 834000, China; zhikeke@cupk.edu.cn

⁴ State Key Laboratory of Heavy Oil Processing—Karamay Branch, Karamay 834000, China

* Correspondence: 006785@xju.edu.cn (L.W.); xjwangdz@sina.com (D.W.); Tel.: +86-13579275610 (L.W.)

† These authors contribute equally to this work.

Abstract: Covalent organic frameworks (COFs) have been widely used in photocatalytic hydrogen peroxide (H₂O₂) production due to their favorable band structure and excellent light absorption. Due to the rapid recombination rate of charge carriers, however, their applications are mainly restricted. This study presents the design and development of two highly conjugated triazine-based COFs (TBP-COF and TTP-COF) and evaluates their photocatalytic H₂O₂ production performance. The nitrogen-rich structures and high degrees of conjugation of TBP-COF and TTP-COF facilitate improved light absorption, promote O₂ adsorption, enhance their redox power, and enable the efficient separation and transfer of photogenerated charge carriers. There is thus an increase in the photocatalytic activity for the production of H₂O₂. When exposed to 10 W LED visible light irradiation at a wavelength of 420 nm, the pyridine-based TTP-COF produced 4244 μmol h⁻¹ g⁻¹ of H₂O₂ from pure water in the absence of a sacrificial agent. Compared to TBP-COF (1882 μmol h⁻¹ g⁻¹), which has a similar structure but lacks pyridine sites, TTP-COF demonstrated nearly 2.5 times greater efficiency. Furthermore, it exhibited superior performance compared to most previously published nonmetal COF-based photocatalysts.

Keywords: imine linked; covalent organic framework; hydrogen peroxide; photocatalysis; two-electron process



Citation: Yang, S.; Zhi, K.; Zhang, Z.; Kerem, R.; Hong, Q.; Zhao, L.; Wu, W.; Wang, L.; Wang, D. Nitrogen-Rich Triazine-Based Covalent Organic Frameworks as Efficient Visible Light Photocatalysts for Hydrogen Peroxide Production. *Nanomaterials* **2024**, *14*, 643. <https://doi.org/10.3390/nano14070643>

Academic Editor: Mohammed Es-Souni

Received: 11 March 2024

Revised: 5 April 2024

Accepted: 6 April 2024

Published: 8 April 2024

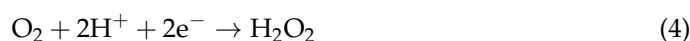
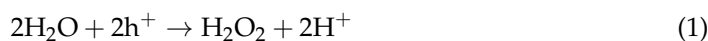


Copyright: © 2024 by the authors. Licensee MDPI, Basel, Switzerland. This article is an open access article distributed under the terms and conditions of the Creative Commons Attribution (CC BY) license (<https://creativecommons.org/licenses/by/4.0/>).

1. Introduction

In recent years, environmental and energy issues have received increasing attention, which has promoted the rapid development of clean energy. Hydrogen peroxide (H₂O₂) is considered a viable sustainable energy source due to its efficiency, versatility, and environmentally friendly oxidant. Therefore, H₂O₂ is widely used in several industries, including chemical synthesis, fuel cells, wastewater treatment, and sterilization [1]. H₂O₂ is traditionally produced on a large scale using anthraquinone oxidation, a process that requires the use of high temperatures and pressures. Moreover, anthraquinone oxidation consumes a significant quantity of costly hydrogen gas and results in the production of hazardous organic by-products [2]. An alternative technique for generating H₂O₂ involves the direct chemical synthesis of H₂ and O₂. However, the O₂ and H₂ gases must be thoroughly diluted with inert gas to avoid an explosion [3]. Due to these factors, a safe, efficient, and clean H₂O₂ generation system is urgently required. Photocatalysis shows excellent potential for the production of H₂O₂. Overall, there are two strategies to achieve H₂O₂

photosynthesis: one involves a water oxidation reaction (WOR), and the other proceeds through the oxygen reduction reaction (ORR) [4]. H_2O_2 can be produced via two photocatalytic WOR routes: one-step direct $2e^-$ processes (Equation (1)) and two-step $2e^-$ processes (Equations (2) and (3)). The photocatalytic ORR generates H_2O_2 through two distinct processes: a one-step direct $2e^-$ reaction (Equation (4)) and a two-step process comprising two $2e^-$ reactions (Equations (5) and (6)) [5].



Currently, the most often used photocatalysts for the production of H_2O_2 are TiO_2 [6], $g\text{-C}_3\text{N}_4$ [7], and some semiconductors [8]. These catalysts are used due to their beneficial characteristics, such as excellent chemical and thermal stability, cost-effectiveness, minimal toxicity, and corrosion resistance. However, their application in the process of H_2O_2 photosynthesis continues to encounter two primary obstacles: (i) The band gaps of these catalysts are relatively broad [9]; (ii) photoinduced e^- and h^+ are rapidly recombined and cannot migrate to their surface to participate in the reaction [10]. Hence, it is crucial to develop highly effective photocatalysts with appropriate photo-redox ability. A characteristic class of reticular materials is known as covalent organic frameworks (COFs), where the molecular building blocks are joined through covalent bonds to form extended structures that can be either two-dimensional (2D) [11] or three-dimensional (3D) [12]. COFs have garnered considerable attention for their well-organized crystalline structure, adaptable topology, and numerous redox-active sites. This has led to significant interest in their application in various fields, including gas storage [13], adsorption [14], energy storage [15], photocatalytic hydrogen production [16], and CO_2 reduction [17]. Specifically, 2D triazine-containing COFs, commonly referred to as covalent triazine frameworks (CTFs), exhibit significant promise in the field of photocatalysis. CTFs have a high nitrogen content, which makes them highly sensitive to visible light. They demonstrate high adjustability, completely conjugated structures, and excellent chemical stability [18]. Xu and colleagues have proven that the presence of acetylene ($-\text{C}\equiv\text{C}-$) or diacetylene ($-\text{C}\equiv\text{C}-\text{C}\equiv\text{C}-$) moieties can greatly enhance the photocatalytic production of H_2O_2 in CTFs [19]. However, the majority of reported CTFs exhibit minimal crystallinity or exist in an amorphous state. This greatly affects the separation of charge carriers and the process of photoexcitation, leading to a decrease in the photocatalytic activity of the carriers [20]. To achieve a highly crystalline structure of COFs, a commonly used method is to directly couple triazine derivatives to other monomers by a Schiff base condensation process. This leads to the formation of an imine-linked 2D COF with a triazine core [21]. For instance, a triazine-structured imine-linked COF was reported by Han et al. Due to its improved crystallinity, broader visible light absorption range, and enhanced charge separation and transfer characteristics, this structure facilitates the efficient photocatalytic generation of H_2O_2 [22]. The catalytic efficiency of COFs for H_2O_2 generation can be greatly improved by rationally adding appropriate sites, such as cyano groups, thioether-decorated sulfone units, piperazine sites, and others. However, COFs continue to require improvements in their photoactivity as a result of restrictions on electron transport within their frameworks, rapid recombination of photogenerated charges, and inefficient generation of intrinsic charges [23]. Therefore, to facilitate electron migration and reduce electron-hole recombination, it is crucial to develop effective strategies for controlling charge separation. Heteroatom doping is an effective method for controlling the optical and electronic characteristics of nanostructures at the

atomic scale. The incorporation of distinct heteroatoms (e.g., N, O, S) into the skeleton of COFs is achieved through the precise design of building blocks [24]. The presence of heteroatoms in the skeleton of COFs inevitably results in a modification of their energy bands, thereby causing effective sites to be introduced and alterations to their electronic and optical properties [25]. Nitrogen doping exhibits notable advantages in various domains when compared to other heteroatoms. Firstly, N and C are adjacent elements in the periodic table and have comparable atomic radii, which prevents the issue of lattice mismatch [26]. Secondly, incorporating N into the structure of COFs not only enhances their inherent physicochemical properties but also significantly improves their surface wettability, electron-donation, electrical conductivity, and reactivity [27]. The presence of a lone pair of electrons on the nitrogen atom in pyridine results in an electron-rich state, developing a partial negative charge on the nitrogen atom. This, in turn, induces a positive charge on the surrounding carbon atoms, leading to a p-type effect. This unique electronic structure contributes to the important role of pyridine nitrogen in different applications. In oxygen reduction catalytic reactions, the pyridine nitrogen is considered to be the active center of the catalytic reaction.

The addition of nitrogen-containing functional groups to a COF skeleton can provide several active sites and significantly enhance photocatalytic performance. In this work, a nitrogen-rich triazine structure was used to prepare an imine-type COF with a high conjugation degree, denoted TBP-COF. To enhance the nitrogen content, an imine-type TTP-COF was synthesized by combining a triazine structure with a pyridine ring. These two COFs demonstrate significantly enhanced abilities to absorb light and have modified energy band structures, resulting in improved production of photocatalytic H₂O₂. TTP-COF is more hydrophilic and nucleophilic due to the nitrogen-rich skeleton structure provided by its triazine and pyridine structures. As a result, TTP-COF produces 4244 μmol h⁻¹ g⁻¹ of H₂O₂ from water in the absence of a sacrificial agent when exposed to 10 W LED visible light irradiation (λ = 420 nm). The efficiency of TTP-COF is approximately 2.5 times more than that of TBP-COF (1882 μmol h⁻¹ g⁻¹), although it has a comparable structure without pyridine sites. This study provides an in-depth comprehension of the systematic development of highly effective catalysts for the photocatalytic synthesis of H₂O₂ from O₂ and water without the need for sacrificial agents. This study illustrates the essential functions of surface hydrophilicity, O₂ adsorption behavior, and the separation of e⁻-h⁺ pairs in controlling the 2e⁻ ORR process.

2. Materials and Methods

2.1. Materials

The materials and reagents involved in this work are described in the Supplementary Materials.

2.2. Preparation of TBP-COF and TTP-COF

2.2.1. Synthesis of TBP-COF

2,4,6-tris(4-bromophenyl)-1,3,5-triazine (TBP-Br): As shown in Figure S1a, in a round bottom flask, 3.54 mL (6 g, 40 mmol) of trifluoromethanesulfonic acid was slowly added to 2 g (11 mmol) of 4-Bromobenzonitrile at 0 °C and stirred for 30 min. The mixture was then stirred at room temperature overnight. After completion of the reaction, the resultant mixture was washed with 100 mL of deionized water, yielding a large amount of white solid precipitate, which was then filtered and collected. The product was purified to yield 1.95 g of a white solid (yield, 99%) [28].

4',4''',4''''-(1,3,5-triazine-2,4,6-triyl) tris (([1,1'-biphenyl]-4-amine)) (TBP-NH₂): As shown in Figure S1b, TBP-Br (0.546 g, 1.0 mmol), 4-aminophenylboronic acid pinacol ester (0.788 g, 3.6 mmol), Pd(PPh₃)₄ (119.0 mg, 0.1 mmol), and K₂CO₃ (0.513 g, 3.72 mmol) were added to a two-neck flask and subjected to a vacuum for 15 min. The mixture was then heated at 110 °C for 14 h with the addition of dioxane (37 mL) and H₂O (5 mL). The solution was poured into a stirring beaker containing ice cubes and H₂O. The solid was separated through

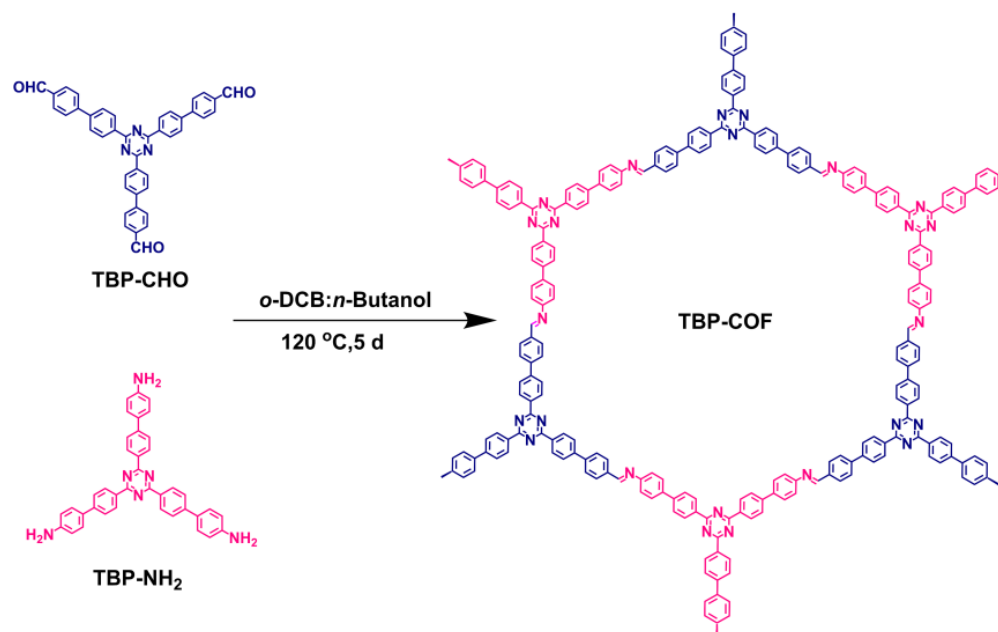
suction filtration, placed in a beaker, and treated with a small amount of methanol (MeOH). Following suction filtration, the undissolved solid was oven-dried for 12 h, yielding 0.472 g of green solid (yield, 81%).

^1H NMR (Figure S8) (600 MHz, DMSO-d_6) δ = 8.73 (d, J = 8.6 Hz, 6H), 7.85 (d, J = 8.6 Hz, 6H), 7.56 (d, J = 8.7 Hz, 6H), 6.71 (d, J = 8.5 Hz, 6H), 5.44 (s, 6H) (Figure S8).

4',4''',4''''-(1,3,5-triazine-2,4,6-triyl) tris ([1,1'-biphenyl]-4-carbaldehyde) (TBP-CHO): As shown in Figure S1c, TBP-Br (0.546 g, 1.0 mmol), 4-formylphenylboronic acid (0.788 g, 3.6 mmol), $\text{Pd}(\text{PPh}_3)_4$ (119.0 mg, 0.1 mmol), and K_2CO_3 (0.513 g, 3.72 mmol) were added in a two-neck flask and placed under vacuum for 15 min. Following the addition of dioxane (37 mL) and H_2O (5 mL), the mixture was heated for 14 h at 110 °C. The mixture was transferred into a stirring beaker containing ice cubes and H_2O . The solid was separated by suction filtration, placed in a beaker, and treated with a small amount of MeOH; the mixture was heated until it boiled, and then sonicated for 15 min. After suction filtration, the undissolved solid was treated with acetone and dried in an oven for 12 h, yielding 0.485 g of gray solid (yield, 78%) [29].

^1H NMR (Figure S9) (600 MHz, TFA) δ = 9.98 (s, 3H), 8.82 (d, J = 8.5 Hz, 6H), 8.15 (d, J = 8.3 Hz, 6H), 8.05 (d, J = 8.5 Hz, 6H), 7.96 (d, J = 8.3 Hz, 6H) (Figure S9).

TBP-COF: In Scheme 1, TBP-CHO (31 mg, 0.05 mmol) and TBP- NH_2 (29 mg, 0.05 mmol) were mixed in 35 mL Pyrex tubes. The solvents *o*-dichlorobenzene (*o*-DCB) and *n*-butanol were added in a 1:1 volume ratio (4 mL). Additionally, acetic acid (6 M, 0.50 mL) was included. The mixture was subjected to ultrasonication for 15 min to achieve uniform dispersion, sealed in a pressure-resistant glass tube, and reacted in an oil bath at 120 °C for 5 d. After the reaction was completed, the reaction tube was cooled to room temperature, and then the crude product was collected and washed three times with *N,N*-Dimethylformamide (DMF), acetone, and tetrahydrofuran (THF). After that, it was dried for 24 h at 100 °C to obtain the green TBP-COF compound (41 mg), with a 68% yield.



Scheme 1. Synthetic routes of TBP-COF.

2.2.2. Synthesis of TTP-COF

2,4,6-tris(5-bromopyridin-2-yl)-1,3,5-triazine (TTP-Br): As shown in Figure S2a, NH_4Br (65 mg) and diisopropylethylamine (113 μL , 0.66 mmol) were added into a round-bottom flask containing a suspension of 5-Bromopicolinonitrile (1.0 g) in 1-pentanol (5 mL). The suspension was heated while being stirred for 12 h in an oil bath at 135 °C. After the reaction, the mixture was cooled to room temperature, resulting in a significant amount of

solid precipitation in the flask. The yellow–white solid (0.8 g) was obtained (yield, 82%) after the solid was collected and filtered, then thoroughly washed with acetonitrile [30].

4,4',4''-((1,3,5-triazine-2,4,6-triyl) tris (pyridine-6,3-diyl)) trianiline (TTP-NH₂): As shown in Figure S2b, TTP-Br (0.549 g, 1.0 mmol), 4-aminophenylboronic acid pinacol ester (0.788 g, 3.6 mmol), Pd(PPh₃)₄ (119.0 mg, 0.1 mmol), CsF (0.547 g, 3.6 mmol), and Cs₂CO₃ (1.212 g, 3.72 mmol) were added to a two-neck flask and kept under vacuum for 15 min. The mixture was then heated at 110 °C for 14 h after adding dioxane (37 mL) and H₂O (5 mL). The solution was poured into a stirring beaker containing ice cubes and H₂O. The solid was separated by suction filtration, transferred to a beaker, and treated with a small amount of MeOH. After suction filtration, the undissolved solid was oven-dried for 12 h, yielding 0.422 g of orange solid (yield, 72%).

¹H NMR (Figure S10) (600 MHz, DMSO-d₆) δ = 9.15 (s, 3H), 8.76 (d, *J* = 8.3 Hz, 3H), 8.26 (d, *J* = 5.9 Hz, 3H), 7.63 (d, *J* = 8.5 Hz, 6H), 6.74 (d, *J* = 8.5 Hz, 6H), 5.56 (s, 6H) (Figure S10).

¹³C NMR (Figure S11) (151 MHz, DMSO-d₆) δ = 171.78, 150.47, 150.27, 147.34, 139.05, 133.17, 128.36, 125.42, 123.16, 114.80, 39.58 (Figure S11).

HRMS *m/z* [M⁺] calculated for C₃₆H₂₈N₉: 586.24622; found: 586.24648.

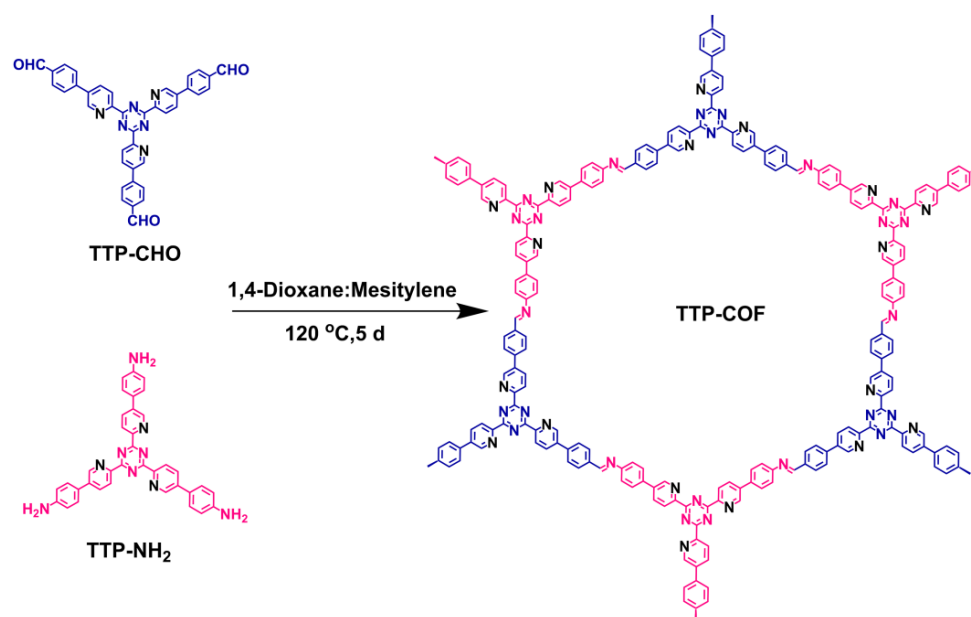
4,4',4''-((1,3,5-triazine-2,4,6-triyl) tris (pyridine-6,3-diyl)) tribenzaldehyde (TTP-CHO): As shown in the Figure S2c, TTP- Br (0.549 g, 1.0 mmol), 4-formylphenylboronic acid (0.788 g, 3.6 mmol), Pd(PPh₃)₄ (119.0 mg, 0.1 mmol), CsF (0.547 g, 3.6 mmol), and Cs₂CO₃ (1.212 g, 3.72 mmol) were added in a two-neck flask and subjected to a vacuum for 15 min. Afterwards, 37 mL of dioxane and 5 mL of H₂O were added, and the mixture was heated to 110 °C for 14 h. The solution was poured into a stirring beaker containing ice cubes and H₂O. The solid was separated by suction filtration, placed in a beaker, and treated with a small amount of MeOH; the mixture was heated till boiling, and then sonicated for 15 min. Following suction filtration, the undissolved solid was dried in an oven for 12 h, yielding 0.487 g of yellow solid (yield, 78%).

¹H NMR (Figure S12) (600 MHz, TFA) δ = 10.11 (s, 3H), 9.74 (d, *J* = 2.2 Hz, 3H), 9.66 (d, *J* = 8.4 Hz, 3H), 9.28 (dd, *J* = 8.4, 2.2 Hz, 3H), 8.32 (d, *J* = 8.4 Hz, 6H), 8.12 (d, *J* = 8.4 Hz, 6H) (Figure S12).

¹³C NMR (Figure S13) (151 MHz, TFA) δ = 192.24, 162.12, 141.98, 140.87, 138.77, 137.31, 134.33, 132.96, 127.66, 124.55, 124.12 (Figure S13).

HRMS *m/z* [M⁺] calculated for C₃₉H₂₅O₃N₆: 625.19827; found: 625.19880.

TTP-COF: As shown in Scheme 2, TTP-CHO (31 mg, 0.05 mmol) and TTP-NH₂ (29 mg, 0.05 mmol) were introduced into 35 mL Pyrex tubes. Subsequently, a mixture of mesitylene:1, 4-dioxane solvents (4 mL, *v:v* = 1:1), and acetic acid (6 M, 0.5 mL) was added. After 15 min of ultrasonication to ensure uniform dispersion, the mixture was sealed in a pressure-resistant glass tube and reacted for 5 d at 120 °C in an oil bath. After the reaction was completed, the reaction tube was cooled to room temperature, and then the crude product was collected and washed three times with DMF, acetone, and THF. It was then dried at 100 °C for 24 h to give the croci TTP-COF compound (49 mg), with a yield of 82%.



Scheme 2. Synthetic routes of TTP-COF.

2.3. Characterization

The ¹H NMR spectra were recorded using a 600 MHz spectrometer (Bruker, Salbrücken, Germany). Solid-state ¹³C NMR spectra were collected using a 400 MHz NMR spectrometer (Bruker, Salbrücken, Germany). An X-ray photoelectron spectrometer (Thermo Scientific K-Alpha, MA, USA) was used to conduct X-ray photoelectron spectroscopy (XPS). The FT-IR spectra were obtained using a Bruker Equinox 55FT-IR spectrometer from Salbrücken, Germany. The spectra were collected in the range of 4000 to 400 cm⁻¹. Powder X-ray diffraction (XRD) patterns were obtained using the Bruker D8 (Salbrücken, Germany). The UV-vis spectrophotometer (U3900, Kyoto, Japan) was used to acquire optical diffuse reflectance spectra at room temperature. A white standard of BaSO₄ was used as the reference. Transmission electron microscopy (TEM) images were obtained using a SU8200 (Kyoto, Japan). An FL spectrofluorometer (F-4500, Kyoto, Japan) was used to collect steady-state photoluminescence (PL) spectra. Meanwhile, time-correlated single photon counting measurements were performed to acquire photoluminescence decay profiles using a single photon counting controller (FLS1000, Edinburgh, UK). The catalyst was subjected to an oxygen temperature-programmed desorption (O₂-TPD) test using an AutoChem1 II 2920 instrument from Norcross, GA, USA. The free radicals of O₂⁻ were recorded using electron paramagnetic resonance (EMX nano, Bruker, Salbrücken, Germany).

2.4. Theoretical Calculation Details

The Vienna Ab initio Simulation Package (VASP) was used to perform all density functional theory (DFT) calculations in the generalized gradient approximation (GGA) with the Perdew–Burke–Ernzerhof (PBE) functional.

The Gibbs free energy (ΔG) for each electrochemical process is calculated as

$$\Delta G = \Delta E + \Delta E_{\text{ZPE}} - T\Delta S = D + D - D$$

where the values of ΔE , ΔE_{ZPE} , and ΔS represent the changes in DFT energy, zero-point energy, and entropy at a specific temperature of 298.15 K, respectively.

2.5. H₂O₂ Detection Methods

A septum was used to seal the tube after 2.5 mg of photocatalyst and 10 mL of water were added. After that, the suspension underwent ultrasonication treatment to disperse

the photocatalyst. The suspension was then allowed to degas for 15 min by bubbling O₂, and to attain absorption–desorption equilibrium, the mixed solution was stirred for 15 min in the dark. The reaction mixture was then illuminated using a 10 W, 420 nm LED. During the experiment, the temperature of the reaction system was carefully controlled at 25 °C using cooling water.

2.6. AQY Measurements

The AQY was calculated as follows:

$$\text{AQY} = \frac{(\text{number of H}_2\text{O}_2 \text{ production}) \times 2}{\text{number of incident photons}} \times 100\%$$

The number of incident photons is

$$N_{\text{incident}} = \frac{Pt}{h\nu} = \frac{Pt\lambda}{hc} = \frac{ISt\lambda}{hc}$$

where I represent the light power intensity (W cm^{-2}), S is the irradiation area (cm^2), t is the reaction time (s), λ is the wavelength length (m) of the monochromatic light, h is the Planck's constant ($6.63 \times 10^{-34} \text{ J s}^{-1}$), and c is the speed of light in free space ($3.0 \times 10^8 \text{ m s}^{-1}$).

3. Results

3.1. Structural Analysis of TBP-COF and TTP-COF

According to the Fourier transform infrared (FT-IR) spectra of TTP-COF and TBP-COF, the stretching peaks associated with $-\text{NH}_2$ ($3100\text{--}3400 \text{ cm}^{-1}$) and $\text{C}=\text{O}$ (1700 cm^{-1}) of the precursors disappeared after synthesis. On the contrary, new peaks (1627 and 1609 cm^{-1}) attributed to the stretching vibration of the $\text{C}=\text{N}$ bond were observed in both COFs. It was demonstrated that the polymerization processes the triazine structure; no changes have occurred in TBP-COF and TTP-COF due to the presence of telescopic vibrational peaks at 1370 and 1352 cm^{-1} , respectively, corresponding to the triazine structure (Figure 1a). This finding supports the successful Schiff base condensation reaction. Powder XRD patterns showed that both COFs are amorphous. Only diffraction peaks corresponding to the partially stacked structures, resulting from the strong $\Pi\text{--}\Pi$ interaction between highly conjugated polymer layers, were found (Figure 1b). The solid-state ^{13}C nuclear magnetic resonance (^{13}C NMR) spectra [31] of TBP-COF and TTP-COF displayed signals at 158 and 162 ppm, corresponding to the carbon atoms of the imine bond (Figure 1c).

The surface area and pore volume of TBP-COF and TTP-COF were analyzed by measuring the nitrogen adsorption–desorption isotherm at 77 K using the Brunauer–Emmett–Teller (BET) method. The BET-specific surface area was calculated using the BET model, resulting in specific surface areas of $73.58 \text{ m}^2 \text{ g}^{-1}$ for TBP-COF and $22.42 \text{ m}^2 \text{ g}^{-1}$ for TTP-COF (Figure S3a), respectively. Furthermore, TBP-COF and TTP-COF had pore diameters of approximately 17.58 nm and 31.13 nm (Figure S3b), as shown by the calculated pore size distributions.

Characteristic peaks of the C, N, and O elements were observed in the elemental composition spectra of TBP-COF (Figure 2a) and TTP-COF (Figure 2d), as determined by XPS. The presence of oxygen and water adsorbed on TBP-COF and TTP-COF could explain the observation of oxygen. The valence states of TBP-COF (Figure 2b,c) and TTP-COF (Figure 2e,f) were analyzed using XPS [32]. This confirmed the successful formation of the desired chemical structures in both COFs.

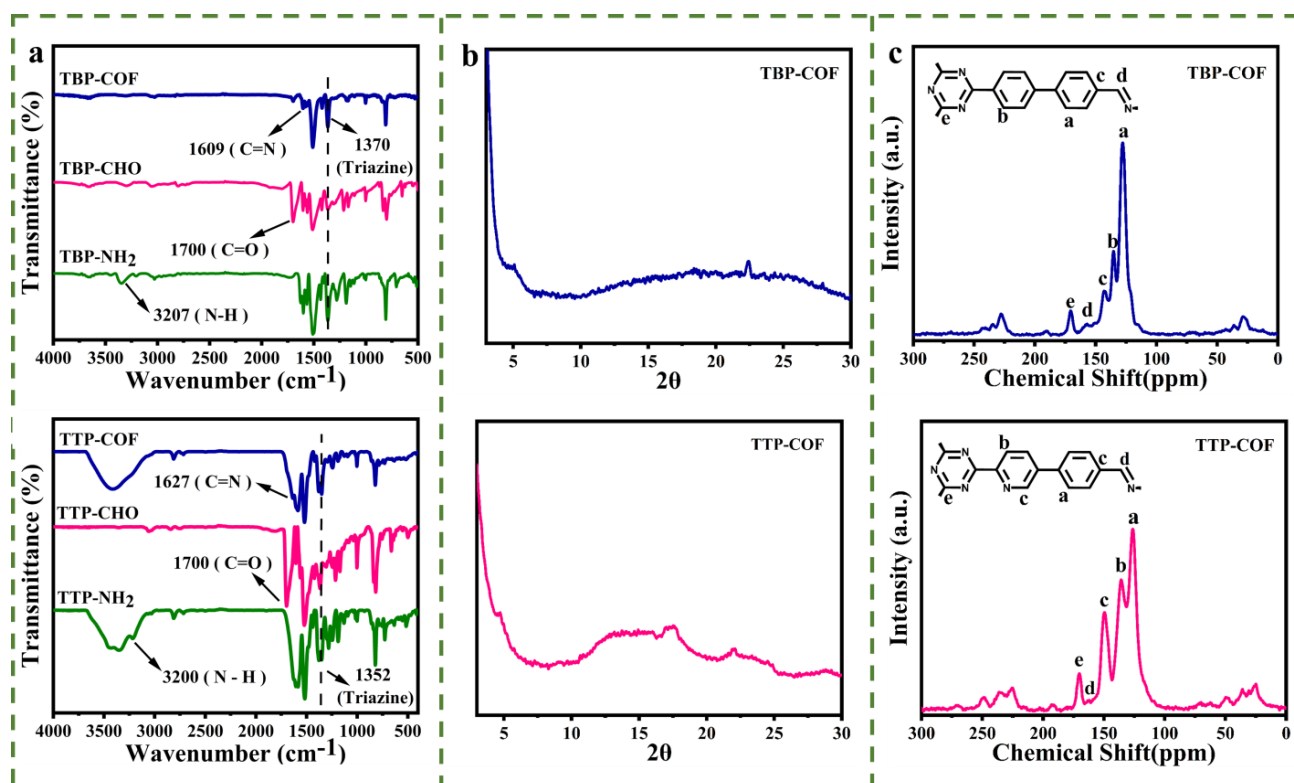


Figure 1. FT-IR spectra of (a) TBP-COF and TTP-COF; (b) XRD patterns of TBP-COF and TTP-COF; (c) ^{13}C NMR spectra and corresponding structures of TBP-COF and TTP-COF.

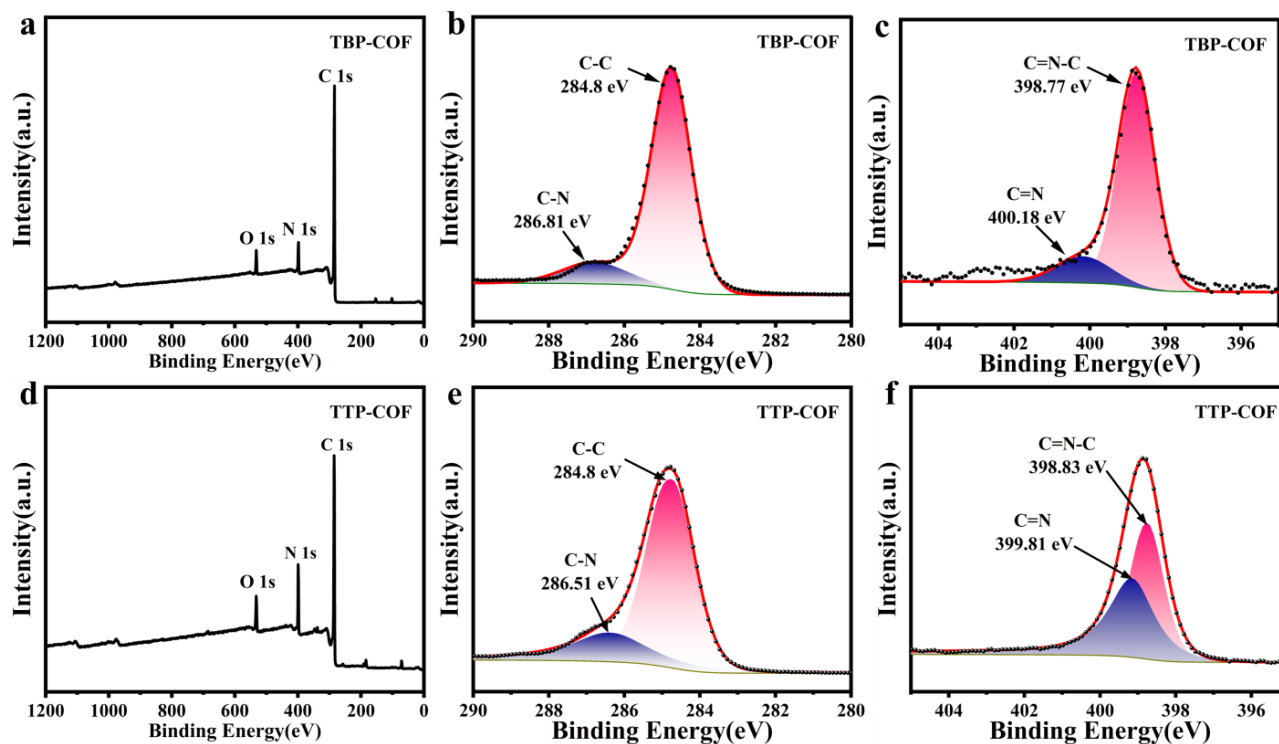


Figure 2. XPS spectra of TBP-COF: (a) survey scan; (b) C 1s; (c) N 1s; XPS spectra of TTP-COF: (d) survey scan; (e) C 1s; (f) N 1s.

The morphology of TBP-COF and TTP-COF was analyzed using scanning electron microscopy (SEM) and transmission electron microscopy (TEM). As illustrated in Figure 3a, TBP-COF displayed a spherical morphology, whereas TTP-COF exhibited a nanosheet-like structure (Figure 3e). The TEM result further confirms that TBP-COF (Figure 3b) and TTP-COF (Figure 3f) are composed of numerous uniform nanostrips. Energy-dispersive X-ray spectroscopy (EDS) was used to confirm the uniform distribution of C and N elements in TBP-COF (Figure 3c,d) and TTP-COF (Figure 3g,h). The thermal stability of TBP-COF and TTP-COF was assessed using thermogravimetric (TG) analysis in a nitrogen atmosphere. TTP-COF showed slight mass loss between 30 °C and 100 °C (Figure S4), which might be related to the decomposition of COF oligomers and the evaporation of a small amount of water [33]. The thermal decomposition of TBP-COF and TTP-COF occurred at temperatures of 550 °C and 500 °C, respectively. In addition, both COFs showed excellent chemical stability in commonly used solvents (Figure S5). The C, H, and N contents of TBP-COF (Table 1) and TTP-COF (Table 2) were found to be in good agreement with the theoretical values, as confirmed by elemental analysis (EA).

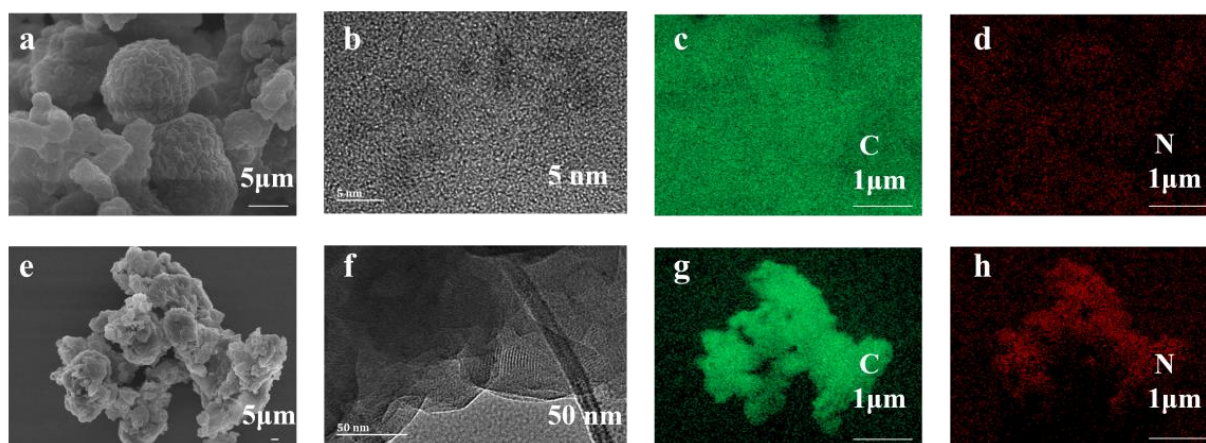


Figure 3. TBP-COF: (a) SEM; (b) TEM; (c,d) EDS. TTP-COF: (e) SEM; (f) TEM; (g,h) EDS.

Table 1. Elemental analysis of TBP-COF.

Element	C%	N%	H%
Theoretical	84.31	10.66	5.03
Experiment	79.17	10.31	2.37

TBP-COF theoretical minimum formulation: $[C_{83}H_{59}N_9]_n$.

Table 2. Elemental analysis of TTP-COF.

Element	C%	N%	H%
Theoretical	77.82	17.68	4.50
Experiment	63.65	15.48	2.66

TTP-COF theoretical minimum formulation: $[C_{77}H_{53}N_{15}]_n$.

3.2. Photocatalytic H_2O_2 Production Performance

As illustrated in Figure 4a, the UV–visible diffuse reflection spectra (UV-vis DRS) of both COFs revealed strong adsorption in the visible spectrum. The band gaps of TTP-COF and TBP-COF were both calculated using Tauc plots and found to be 2.05 eV and 2.50 eV, respectively (Figure 4b). TTP-COF exhibits a lower band gap and a broader range of visible light absorption due to the presence of a pyridine ring, in contrast to TBP-COF. This characteristic is advantageous for the photocatalytic production of H_2O_2 . The electrochemical Mott–Schottky plots of both COFs (Figure 4c) displayed positive slopes,

suggesting that they possess the characteristics of n-type semiconductors [34]. TBP-COF showed a flat band potential of -0.35 V (vs. Ag/AgCl), while TTP-COF had a flat band potential of -0.50 V (vs. Ag/AgCl). The valence band (VB) and conduction band (CB) were determined using the band gap and flat band calculations (Figure 4d). The results confirm that COFs have the ability to facilitate the 2e-ORR pathway, thereby ensuring a significant increase in H_2O_2 production (Figure 4e).

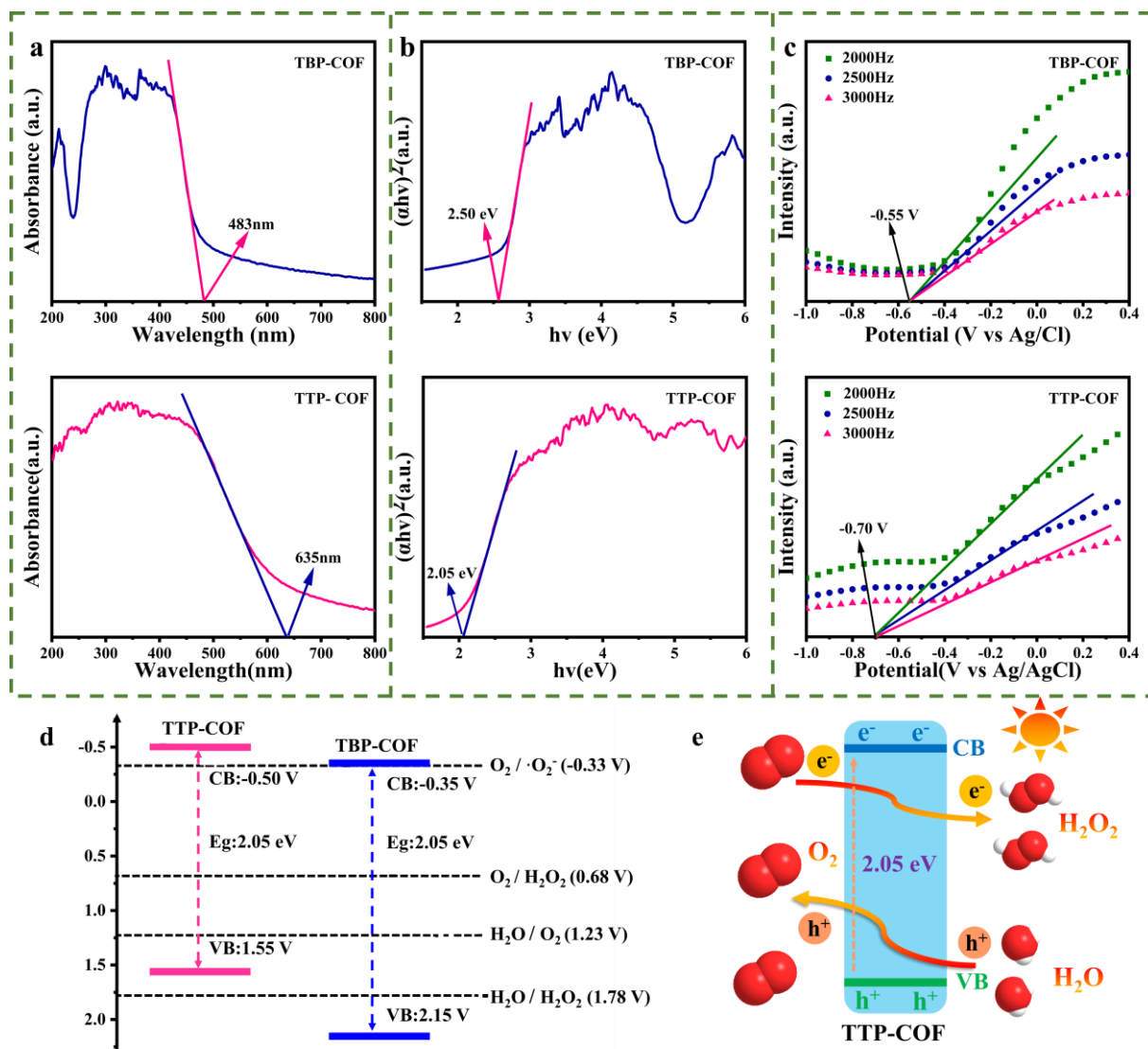


Figure 4. UV-DRS plots of (a) TBP-COF and TTP-COF; Tauc plots of (b) TBP-COF and TTP-COF; Mott-Schottky plots of (c) TBP-COF and TTP-COF; (d) band alignment of TBP-COF and TTP-COF; (e) overall H_2O_2 photosynthesis over TTP-COF.

In the absence of any sacrificial reagent, the photocatalytic activity of the COFs in producing H_2O_2 was evaluated in water and O_2 under 10 W LED visible light irradiation. Figure 5a illustrates that when exposed to 10 W LED visible light irradiation ($\lambda = 420$ nm), TBP-COF produced a moderate amount of H_2O_2 ($1882 \mu\text{mol h}^{-1} \text{g}^{-1}$). The pyridine-containing structure TTP-COF increased the rate of H_2O_2 production by $4244 \mu\text{mol h}^{-1} \text{g}^{-1}$. Therefore, pyridine is essential for enhancing the activity of COFs towards H_2O_2 . Figure 5b,c and Table S1 demonstrate that TTP-COF had superior performance compared to most other metal-free photocatalysts under LED visible light conditions in pure water for the production of H_2O_2 . Furthermore, it outperformed most catalysts with

sacrificial agents [19,23,35–38]. Thus, TTP-COF is identified as one of the most effective COF-based catalysts for photocatalytic H_2O_2 generation. To further examine the performance of TTP-COF in the production of H_2O_2 , the dosage of the catalyst was examined. It can be observed from Figure 5d that the highest H_2O_2 production occurs at an optimal TTP-COF concentration of 0.25 g L^{-1} ; however, as the TTP-COF concentration is increased, the H_2O_2 concentration decreases. This is primarily attributed to the hindrance of light absorption and utilization caused by an excessively high catalyst concentration [39]. The photocatalytic pathway of H_2O_2 production over the COFs was elucidated through a series of contrast experiments. The photocatalytic performance of the COFs studied in the dark and under different atmospheric conditions ($\text{N}_2/\text{Air}/\text{O}_2$) is displayed in Figure 5e. H_2O_2 is produced via photocatalytic oxygen reduction, as almost no H_2O_2 was detected in an N_2 -saturated solution or under dark conditions [40]. In addition, quenching experiments were performed to gain insight into the role of reactive species, as illustrated in Figure 5f. KBrO_3 , MeOH, and p-benzoquinone (p-BQ) were employed as scavengers for e^- , h^+ , and $\cdot\text{O}_2^-$, respectively [41]. The findings indicated that the H_2O_2 production of TTP-COF and TBP-COF significantly decreased when electrons and $\text{O}_2^{\cdot-}$ were quenched, indicating that the ORR plays a crucial role in this photocatalytic system [42].

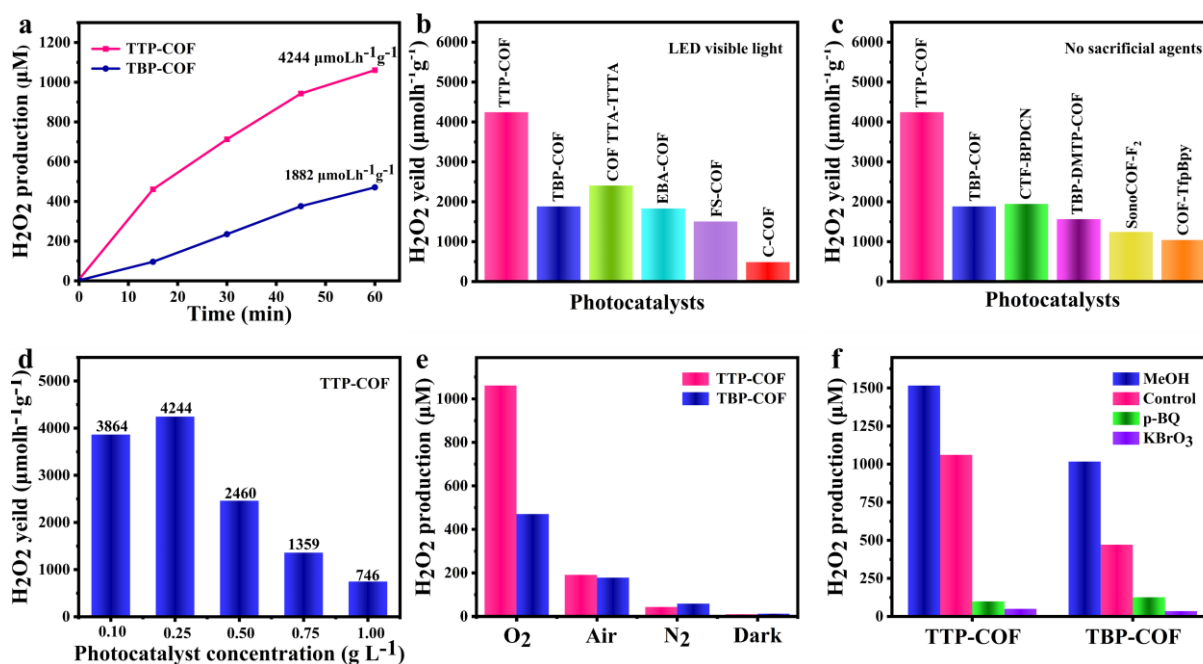


Figure 5. (a) Time-dependent H_2O_2 photogeneration of TBP-COF and TTP-COF under 420 nm LED visible light; (b) the photocatalytic properties of TBP-COF and TTP-COF compared with other photocatalysts under LED visible light conditions; (c) the photocatalytic properties of TBP-COF and TTP-COF compared with other photocatalysts without sacrificial agents; (d) photocatalytic H_2O_2 yield of TTP-COF with different catalyst concentrations; (e) H_2O_2 production of TBP-COF and TTP-COF under different conditions (dark, N_2 , air, O_2); (f) comparison of H_2O_2 production by TBP-COF and TTP-COF under different conditions.

H_2O_2 is known to have poor stability, especially under light irradiation. Therefore, the decomposition of H_2O_2 on the developed catalysts was also investigated. The lack of significant variation in the concentration of the H_2O_2 aqueous solution when both COF catalysts are present suggests that the distinct H_2O_2 generation characteristics of the catalysts cannot be ascribed to differences in H_2O_2 decomposition (Figure 6a). At 420 nm, TBP-COF had an apparent quantum yield of 1% (Figure 6b), while the apparent quantum yield of TTP-COF was 5.2% (Figure 6c). After undergoing four rounds of irradiation, the recycling test results demonstrated that both TBP-COF and TTP-COF maintained a

significantly high level of photocatalytic performance (Figure 6d). Furthermore, the FT-IR spectra showed no noticeable changes after the reaction. (Figure 6e,f). The characteristic peaks of C 1s, N 1s, and O 1s in TBP-COF and TTP-COF, as shown in Figure S6, did not show any noticeable peak shifts during the photocatalytic reaction. This provides further evidence of the structural integrity of the frameworks without decomposition. The morphology of TBP-COF and TTP-COF following photocatalysis was analyzed using SEM and TEM. TBP-COF retained its spherical form, but TTP-COF exhibited a nanosheet structure (Figure S7). EDS measurements revealed a homogenous distribution of C and N elements. However, the sizes of TBP-COF and TTP-COF exhibited increased surface roughness, thereby facilitating the scattering of incident light and enhancing light absorption capabilities [43]. These findings indicate that TBP-COF and TTP-COF demonstrate excellent stability in continuous H_2O_2 production, making them highly promising for real-time applications.

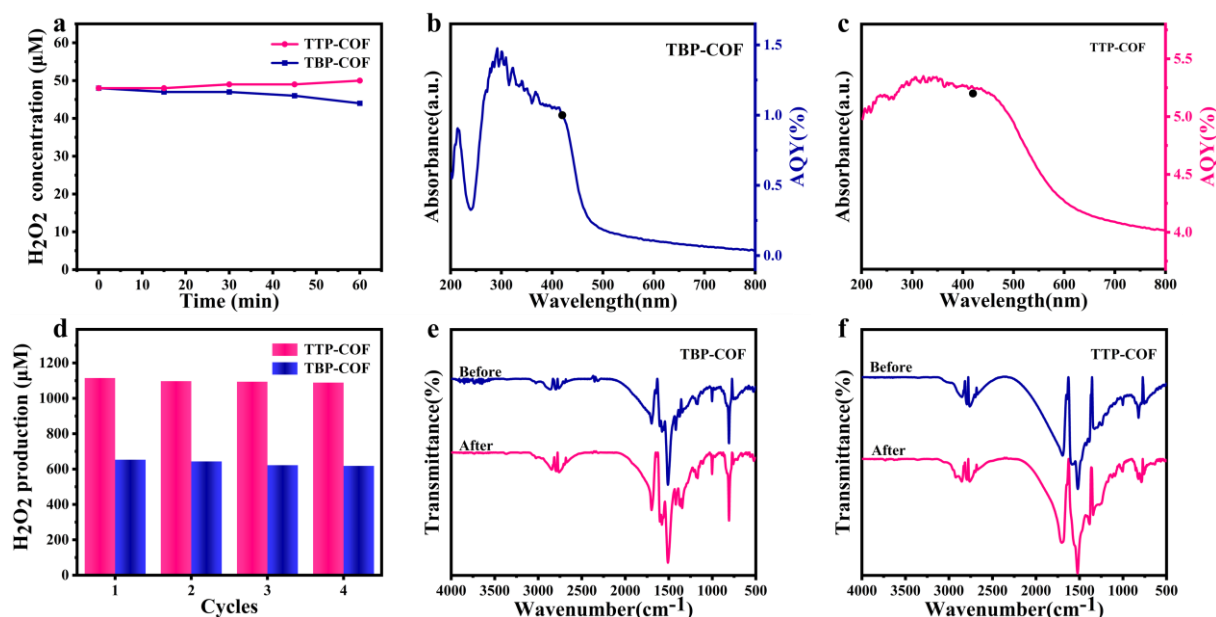


Figure 6. (a) The decomposition of H_2O_2 by COFs; AQY of (b) TBP-COF and (c) TTP-COF; (d) recycling H_2O_2 production on TBP-COF and TTP-COF; FT-IR spectra of (e) TBP-COF and (f) TTP-COF obtained before and after photocatalytic recycles.

Dimethyl-1-pyrroline N-oxide (DMPO) was used as a spin-trap agent to obtain electron paramagnetic resonance (EPR) spectra. This facilitated the determination of the active oxygen species participating in the photocatalytic process [44]. The spectra of TTP-COF and TBP-COF displayed distinct peaks associated with $DMPO-O_2^{\cdot-}$ when exposed to visible light (Figure 7a). This suggests that $O_2^{\cdot-}$ was generated as an intermediate species. Furthermore, this result suggests that H_2O_2 is produced by this photocatalytic system via a $2e^-$ two-step ORR mechanism ($O_2 \rightarrow O_2^{\cdot-} \rightarrow H_2O_2$). The O_2 and H_2O uptake performance of TBP-COF and TTP-COF was analyzed to understand the mechanism behind the enhanced catalytic performance of TBP-COF and TTP-COF for H_2O_2 production. The obtained O_2 temperature-programmed desorption (O_2 -TPD) curves demonstrated that TTP-COF shows a more pronounced O_2 desorption peak in comparison to TBP-COF (Figure 7b). Therefore, the pyridine-containing TTP-COF exhibits an enhanced chemical adsorption capacity for O_2 [45]. In addition, because of the hydrophilic and nucleophilic properties of pyridine, the zeta potential (Figure 7c) and hydrophilicity (Figure 7d,e) of TTP-COF were significantly greater than those of TBP-COF. Furthermore, the hydrophilic and nucleophilic characteristics of pyridine [38] contribute to the increased chemisorption of O_2 and enhanced hydrophilicity of TTP-COF, hence promoting the generation of H_2O_2 during the ORR process. To acquire more comprehensive insights into the charge transport mechanisms and

visible light reactions of TBP-COF and TTP-COF, the electrochemical impedance spectra (EIS) and transient photocurrent responses of the photocatalysts were measured under light illumination [46]. The Nyquist curve of TTP-COF demonstrated a reduced diameter of the semicircle in comparison to TBP-COF (Figure 7f). This suggests that the pyridine group modification efficiently accelerates the kinetics of interfacial charge transport [47]. As demonstrated in Figure 7g, the introduction of pyridine increased the generation of photoexcited charges and facilitated the separation of photogenerated $e^- - h^+$ as a result of the lower photocurrent density of TBP-COF in comparison to TTP-COF. Time-resolved photoluminescence (TRPL) and photoluminescence (PL) spectroscopy were employed to analyze the behavior of photogenerated carriers in the two COFs. The PL intensity of TTP-COF was somewhat quenched in contrast to TBP-COF (Figure 7h), suggesting suppressed recombination of photogenerated electrons and holes [48]. Compared to TTP-COF ($\tau_{Ave.} = 1.54$ ns), TBP-COF exhibited a significantly longer average lifetime ($\tau_{Ave.} = 4.20$ ns), as illustrated in Figure 7i. The reduced lifetime suggests improved separation of electrons and holes, indicating that the photogenerated carriers are effectively captured by reactive substrates, enabling them to facilitate redox reactions [49]. The findings of this study indicate that the pyridine group modification accelerates interfacial charge transport kinetics and facilitates the separation of photogenerated carriers. As a result, TTP-COF demonstrates improved photocatalytic efficacy in the production of H_2O_2 .

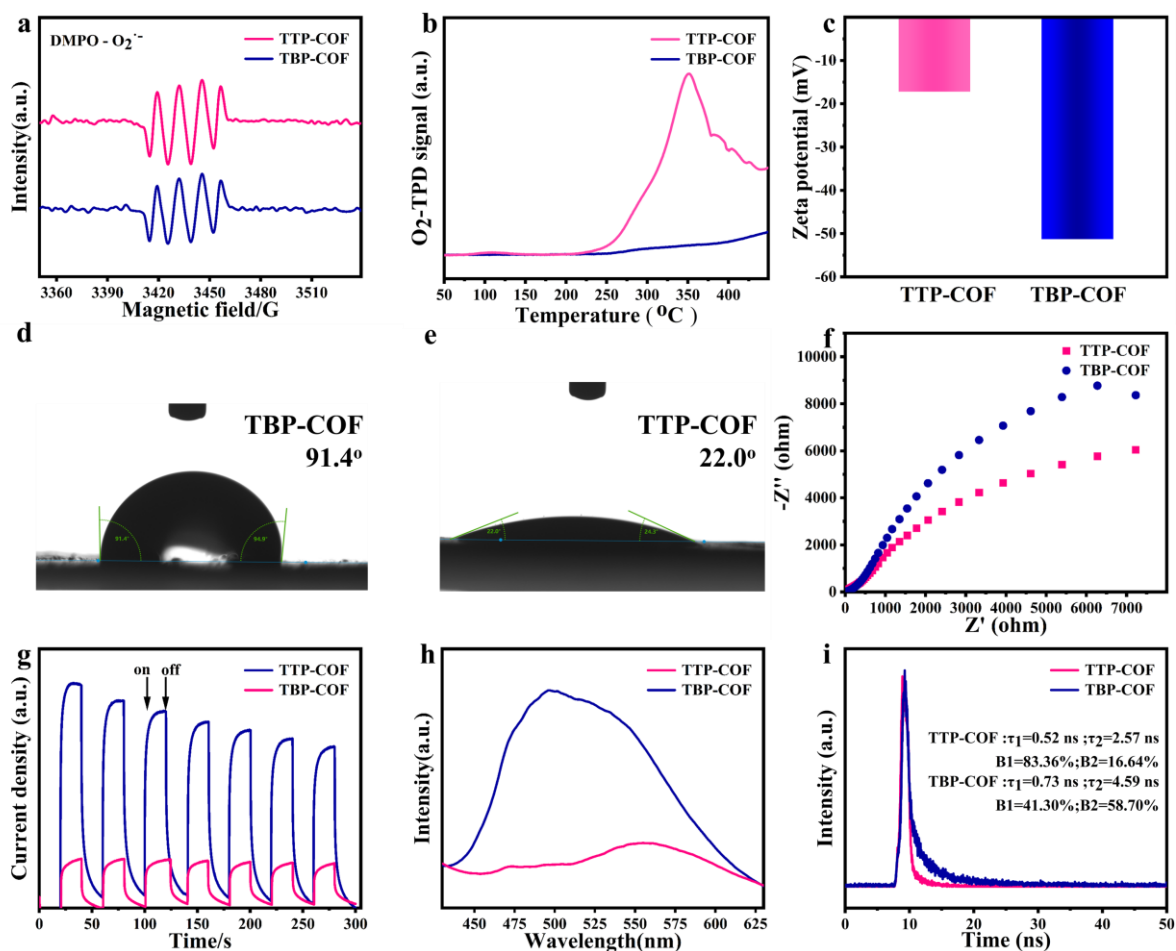


Figure 7. (a) EPR spectra of TBP-COF and TTP-COF; (b) O_2 -TPD curves of TBP-COF and TTP-COF; (c) the Zeta potential of TBP-COF and TTP-COF; water contact angle patterns of (d) TBP-COF and (e) TTP-COF; (f) EIS curves of TBP-COF and TTP-COF; (g) photocurrent responses of TBP-COF and TTP-COF; (h) PL spectra of TBP-COF and TTP-COF; (i) TRPL spectra of TBP-COF and TTP-COF.

Quantum chemical modeling was conducted using the density functional theory (DFT) method to investigate the adsorption performance of the catalyst and the effect of the composition and structure of the material on the kinetics of the catalytic process [50]. Theoretical calculations provided additional insight into the role of the pyridine ring in facilitating the photocatalytic $2e^-$ two-step ORR performance of COFs in the production of H_2O_2 . The benefits of these catalysts in photocatalytic H_2O_2 production are determined by the interaction between OOH^* intermediates and the active sites on the catalyst surface (Figure 8a,b). Figure 8c demonstrates that the energy barrier of the OOH^* intermediate in TTP-COF was lowered by 0.898 eV compared to TBP-COF. This indicates that modifying the pyridine ring of the COFs can enhance the binding strength of OOH^* intermediates to the active sites [51], leading to highly effective photocatalytic activity for the production of H_2O_2 .

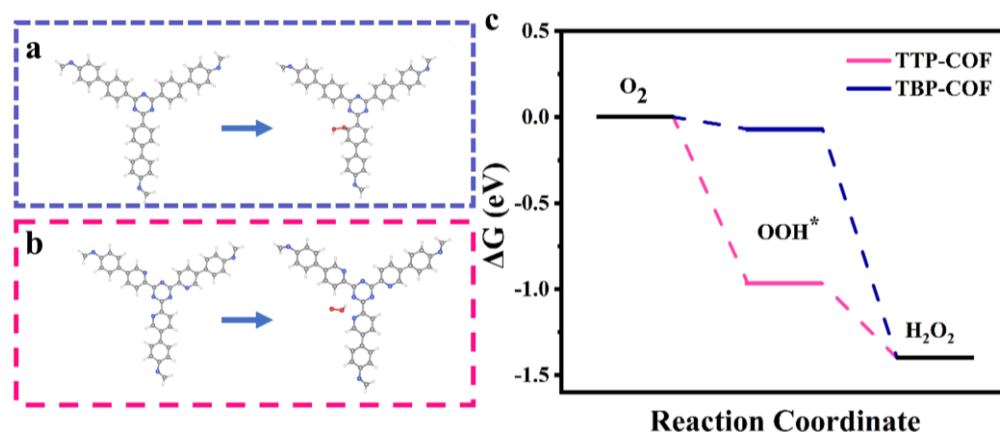


Figure 8. (a) The benzene ring acts as an active site in TBP-COF (C: gray, N: blue, O: red, H: white); (b) the pyridine ring acts as an active site in TTP-COF (C: gray, N: blue, O: red, H: white); (c) free energy diagrams of H_2O_2 generation pathways.

4. Conclusions

In summary, two triazine-based COFs (TBP-COF and TTP-COF) were designed and synthesized with a focus on achieving efficient photocatalytic production of H_2O_2 from H_2O and O_2 . TTP-COF demonstrated excellent photocatalytic performance because of its strong light absorption, nitrogen-rich triazine and pyridine rings, and an appropriate band structure for photocatalytic H_2O_2 generation. The TTP-COF catalyst achieved an H_2O_2 production of $4244 \mu\text{mol h}^{-1} \text{g}^{-1}$ without requiring additional cocatalysts or sacrificial agents. In addition, TTP-COF demonstrated excellent cyclic stability, retaining its structural and chemical characteristics effectively after photocatalytic cycling tests. Pyridine significantly altered the band structure of TTP-COF and expanded its visible light absorption, making it more appropriate for the $2e^-$ two-step ORR process. This increased the overall photogeneration of H_2O_2 . The DFT calculations of TBP-COF and TTP-COF demonstrate that including a pyridine ring is advantageous for enhancing photocatalytic performance. This work demonstrates that the degree of conjugation and nitrogen content of COFs can be enhanced to achieve optimal overall photocatalytic H_2O_2 generation. This study also provides valuable insights into the design and development of COF-based catalysts for the photosynthesis of chemical fuel.

Supplementary Materials: The following supporting information can be downloaded at: <https://www.mdpi.com/article/10.3390/nano14070643/s1>, Figure S1: synthesis routes of (a) TBP-Br; (b) TBP-NH₂; (c) TBP-CHO; Figure S2: synthesis routes of (a) TTP-Br; (b) TTP-NH₂; (c) TTP-CHO; Figure S3: TBP-COF and TTP-COF: (a) N₂ sorption isotherms at 77 K; (b) pore size distributions; Figure S4: TG curves of TBP-COF and TTP-COF under N₂ atmosphere; Figure S5: FT-IR patterns of (a) TBP-COF and (b) TTP-COF samples treated at room temperature for 24 h in 1 M of HCl, 1 M of NaOH, H₂O and DMF. The chemical stability of the COFs was evaluated by soaking the COFs in

various solvents such as HCl, NaOH, H₂O and DMF at concentrations of 0.5 g L⁻¹; Figure S6: XPS spectra of TBP-COF after photocatalysis: (a) Survey scan; (b) C 1s; (c) N 1s; XPS spectra of TTP-COF after photocatalysis: (d) Survey scan; (e) C 1s; (f) N 1s; Figure S7: TBP-COF after photocatalysis: (a) SEM; (b) TEM; (c and d) EDS; TTP-COF after photocatalysis: (e) SEM; (f) TEM; (g and h) EDS; Figure S8: ¹H NMR spectra of TBP-NH₂; Figure S9: ¹H NMR spectra of TBP-CHO; Figure S10: ¹H NMR spectra of TTP-NH₂; Figure S11: ¹³C NMR spectra of TTP-NH₂; Figure S12: ¹H NMR spectra of TTP-CHO; Figure S13: ¹³C NMR spectra of TTP-CHO; Table S1: Comparison of photocatalytic H₂O₂ performance on various representative photocatalysts. (See Refs. [19,21–23,35–38,44,52]).

Author Contributions: Conceptualization, S.Y. and K.Z.; methodology, S.Y. and K.Z.; software, Z.Z. and R.K.; validation, S.Y., Z.Z. and Q.H.; formal analysis, Q.H. and L.Z.; investigation, S.Y., K.Z. and W.W.; resources, L.Z. and W.W.; data curation, S.Y., K.Z. and Z.Z.; writing—original draft preparation, S.Y.; writing—review and editing, L.W. and D.W.; visualization, L.Z. and W.W.; supervision, L.W. and D.W.; project administration, L.W. and D.W.; funding acquisition, K.Z. and L.W. All authors contributed substantially to the work reported. All authors have read and agreed to the published version of the manuscript.

Funding: This research was sponsored by the Natural Science Foundation of the Xinjiang Uygur Autonomous Region, grant number 2022D01F36. PhD Research Start-up Foundation of Xinjiang University (No. BS190242).

Data Availability Statement: The data presented in this study are available on request from the corresponding author.

Conflicts of Interest: The authors declare no conflicts of interest.

References

1. Zhao, Y.; Li, X.K.; Fan, X.; Wang, H.S.; Liu, Y.L.; Chen, Y.Y.; Yang, T.Y.; Ye, J.; Huang, H.; Li, H.T.; et al. Small-Molecule Catalyzed H₂O₂ Production via a Phase-Transfer Photocatalytic Process. *Appl. Catal. B-Environ.* **2022**, *314*, 121499. [[CrossRef](#)]
2. Guo, Y.Y.; Dai, C.N.; Lei, Z.G.; Chen, B.H.; Fang, X.C. Synthesis of Hydrogen Peroxide over Pd/SiO₂/COR Monolith Catalysts by Anthraquinone Method. *Catal. Today* **2016**, *276*, 36–45. [[CrossRef](#)]
3. Urban, S.; Weltin, A.; Flamm, H.; Kieninger, J.; Deschner, B.J.; Kraut, M.; Dittmeyer, R.; Urban, G.A. Electrochemical Multisensor System for Monitoring Hydrogen Peroxide, Hydrogen and Oxygen in Direct Synthesis Microreactors. *Sens. Actuat. B-Chem.* **2018**, *273*, 973–982. [[CrossRef](#)]
4. Tan, D.; Zhuang, R.; Chen, R.; Ban, M.; Feng, W.; Xu, F.; Chen, X.; Wang, Q. Covalent Organic Frameworks Enable Sustainable Solar to Hydrogen Peroxide. *Adv. Funct. Mater.* **2023**, *34*, 202311655. [[CrossRef](#)]
5. Zhou, Z.M.; Sun, M.H.; Zhu, Y.B.; Li, P.Z.; Zhang, Y.R.; Wang, M.K.; Shen, Y. A Thioether-Decorated Triazine-Based Covalent Organic Framework Towards Overall H₂O₂ Photosynthesis without Sacrificial Agents. *Appl. Catal. B-Environ.* **2023**, *334*, 122862. [[CrossRef](#)]
6. Zhao, Y.F.; Kondo, Y.; Kuwahara, Y.; Mori, K.; Yamashita, H. Hydrophobic and Visible-Light Responsive Tio as an Efficient Photocatalyst for Promoting Hydrogen Peroxide Production in a Two-Phase System. *Catal. Today* **2024**, *425*, 114350. [[CrossRef](#)]
7. Mahvelati-Shamsabadi, T.; Fattahimoghaddam, H.; Lee, B.K.; Bae, S.; Ryu, J. Synthesis of Hexagonal Rosettes of g-C₃N₄ with Boosted Charge Transfer for the Enhanced Visible-Light Photocatalytic Hydrogen Evolution and Hydrogen Peroxide Production. *J. Colloid Interf. Sci.* **2021**, *597*, 345–360. [[CrossRef](#)]
8. Yang, D.; Li, Y.; Chen, R.; Wang, X.; Li, Z.; Xing, T.; Wei, L.; Xu, S.; Dai, P.; Wu, M. Flower-Like Superstructure of Boron Carbon Nitride Nanosheets with Adjustable Band Gaps for Photocatalytic Hydrogen Peroxide Production. *J. Mater. Sci. Technol* **2024**, *183*, 23–31. [[CrossRef](#)]
9. Yang, C.; Qian, C.; Yu, M.; Liao, Y. Manipulation of Band Gap and Hydrophilicity in Vinylene-Linked Covalent Organic Frameworks for Improved Visible-Light-Driven Hydrogen Evolution by End-Capping Strategy. *Chem. Eng. J.* **2023**, *454*, 140341. [[CrossRef](#)]
10. Sun, K.; Shen, J.; Liu, Q.; Tang, H.; Zhang, M.; Zulfiqar, S.; Lei, C. Synergistic Effect of Co(II)-Hole and Pt-Electron Cocatalysts for Enhanced Photocatalytic Hydrogen Evolution Performance of P-Doped g-C₃N₄. *Chin. J. Catal.* **2020**, *41*, 72–81. [[CrossRef](#)]
11. Naberezhnyi, D.; Park, S.; Li, W.; Westphal, M.; Feng, X.; Dong, R.; Dementyev, P. Mass Transfer in Boronate Ester 2D COF Single Crystals. *Small* **2021**, *17*, e2104392. [[CrossRef](#)] [[PubMed](#)]
12. Borkowska, M.; Mrówczyński, R. Triptycene Based 3D Covalent Organic Frameworks (COFs)—An Emerging Class of 3D Structures. *Symmetry* **2023**, *15*, 1803. [[CrossRef](#)]
13. Mow, R.E.; Russell-Parks, G.A.; Redwine, G.E.B.; Petel, B.E.; Gennett, T.; Braunecker, W.A. Polymer-Coated Covalent Organic Frameworks as Porous Liquids for Gas Storage. *Chem. Mater.* **2024**, *36*, 1579–1590. [[CrossRef](#)] [[PubMed](#)]
14. Liang, L.; Chen, J.; Chen, X.; Wang, J.; Qiu, H. In Situ Synthesis of a GO/COFs Composite with Enhanced Adsorption Performance for Organic Pollutants in Water. *Environ. Sci. Nano* **2022**, *9*, 554–567. [[CrossRef](#)]

15. He, Y.; An, N.; Meng, C.; Xie, K.; Wang, X.; Dong, X.; Sun, D.; Yang, Y.; Hu, Z. High-Density Active Site COFs with a Flower-Like Morphology for Energy Storage Applications. *J. Mater. Chem. A* **2022**, *10*, 11030–11038. [[CrossRef](#)]
16. Chen, C.X.; Xiong, Y.Y.; Zhong, X.; Lan, P.C.; Wei, Z.W.; Pan, H.; Su, P.Y.; Song, Y.; Chen, Y.F.; Nafady, A.; et al. Enhancing Photocatalytic Hydrogen Production Via the Construction of Robust Multivariate Ti-MOF/COF Composites. *Angew. Chem. Int. Ed. Engl.* **2022**, *61*, e202114071. [[CrossRef](#)] [[PubMed](#)]
17. Yang, X.; Lan, X.; Zhang, Y.; Li, H.; Bai, G. Rational Design of MoS₂@COF Hybrid Composites Promoting C-C Coupling for Photocatalytic CO₂ Reduction to Ethane. *Appl. Catal. B* **2023**, *325*, 122393. [[CrossRef](#)]
18. Sun, R.X.; Tan, B.E. Covalent Triazine Frameworks(CTFs) for Photocatalytic Applications. *Chem. Res. Chin. Univ.* **2022**, *38*, 310–324. [[CrossRef](#)]
19. Chen, L.; Wang, L.; Wan, Y.; Zhang, Y.; Qi, Z.; Wu, X.; Xu, H. Acetylene and Diacetylene Functionalized Covalent Triazine Frameworks as Metal-Free Photocatalysts for Hydrogen Peroxide Production: A New Two-Electron Water Oxidation Pathway. *Adv. Mater.* **2020**, *32*, e1904433. [[CrossRef](#)]
20. Wang, H.; Wang, H.; Wang, Z.; Tang, L.; Zeng, G.; Xu, P.; Chen, M.; Xiong, T.; Zhou, C.; Li, X.; et al. Covalent Organic Framework Photocatalysts: Structures and Applications. *Chem. Soc. Rev.* **2020**, *49*, 4135–4165. [[CrossRef](#)]
21. Tan, F.; Zheng, Y.; Zhou, Z.; Wang, H.; Dong, X.; Yang, J.; Ou, Z.; Qi, H.; Liu, W.; Zheng, Z.; et al. Aqueous Synthesis of Covalent Organic Frameworks as Photocatalysts for Hydrogen Peroxide Production. *CCS Chem.* **2022**, *4*, 3751–3761. [[CrossRef](#)]
22. Wang, H.; Yang, C.; Chen, F.; Zheng, G.; Han, Q. A Crystalline Partially Fluorinated Triazine Covalent Organic Framework for Efficient Photosynthesis of Hydrogen Peroxide. *Angew. Chem. Int. Ed. Engl.* **2022**, *61*, e202202328. [[CrossRef](#)] [[PubMed](#)]
23. Zhai, L.; Xie, Z.; Cui, C.-X.; Yang, X.; Xu, Q.; Ke, X.; Liu, M.; Qu, L.-B.; Chen, X.; Mi, L. Constructing Synergistic Triazine and Acetylene Cores in Fully Conjugated Covalent Organic Frameworks for Cascade Photocatalytic H₂O₂ Production. *Chem. Mater.* **2022**, *34*, 5232–5240. [[CrossRef](#)]
24. Yang, L.; Song, Y.; Li, J.; Xu, W.; Peng, C.; Wang, L. S,N-Rich Luminous Covalent Organic Frameworks for Hg²⁺ Detection and Removal. *Chemosphere* **2023**, *311*, 136919. [[CrossRef](#)] [[PubMed](#)]
25. Wang, H.; Shao, Y.; Mei, S.; Lu, Y.; Zhang, M.; Sun, J.-k.; Matyjaszewski, K.; Antonietti, M.; Yuan, J. Polymer-Derived Heteroatom-Doped Porous Carbon Materials. *Chem. Rev.* **2020**, *120*, 9363–9419. [[CrossRef](#)]
26. Wood, K.N.; O'Hayre, R.; Pylypenko, S. Recent Progress on Nitrogen/Carbon Structures Designed for Use in Energy and Sustainability Applications. *Energy Environ. Sci.* **2014**, *7*, 1212–1249. [[CrossRef](#)]
27. Ismagilov, Z.R.; Shalagina, A.E.; Podyacheva, O.Y.; Ischenko, A.V.; Kibis, L.S.; Boronin, A.I.; Chesalov, Y.A.; Kochubey, D.I.; Romanenko, A.I.; Anikeeva, O.B.; et al. Structure and Electrical Conductivity of Nitrogen-Doped Carbon Nanofibers. *Carbon* **2009**, *47*, 1922–1929. [[CrossRef](#)]
28. Liu, Z.; Su, Q.; Ju, P.; Li, X.; Li, G.; Wu, Q.; Yang, B. A Hydrophilic Covalent Organic Framework for Photocatalytic Oxidation of Benzylamine in Water. *Chem. Commun.* **2020**, *56*, 766–769. [[CrossRef](#)] [[PubMed](#)]
29. Bi, S.; Zhang, Z.; Meng, F.; Wu, D.; Chen, J.S.; Zhang, F. Heteroatom-Embedded Approach to Vinylene-Linked Covalent Organic Frameworks with Isoelectronic Structures for Photoredox Catalysis. *Angew. Chem. Int. Ed. Engl.* **2021**, *61*, e202111627. [[CrossRef](#)]
30. Frost, J.M.; Kobera, L.; Pialat, A.; Zhang, Y.; Southern, S.A.; Gabidullin, B.; Bryce, D.L.; Murugesu, M. From Discrete Molecule, to Polymer, to Mof: Mapping the Coordination Chemistry of Cd using ¹¹³Cd Solid-State Nmr. *Chem. Commun.* **2016**, *52*, 10680–10683. [[CrossRef](#)]
31. Zhou, S.; Hu, H.; Hu, H.; Jiang, Q.; Xie, H.; Li, C.; Gao, S.; Kong, Y.; Hu, Y. Unveiling the Latent Reactivity of Imines on Pyridine-Functionalized Covalent Organic Frameworks for H₂O₂ Photosynthesis. *China Mater.* **2023**, *66*, 1837–1846. [[CrossRef](#)]
32. Chen, X.; Li, Y.; Jia, L.; Yu, X.; Wang, Q.; Zhang, Y.; Zhang, Z.; Liang, E.; Han, B.; Li, J. N-Doping and Structural Regularity of Covalent Organic Frameworks (COFs) Tune the Catalytic Activity for Knoevenagel Condensation Reaction. *J. Solid State Chem.* **2023**, *328*, 124352. [[CrossRef](#)]
33. Zhai, S.; Lu, Z.; Ai, Y.; Jia, X.; Yang, Y.; Liu, X.; Tian, M.; Bian, X.; Lin, J.; He, S. High Performance Nanocomposite Proton Exchange Membranes Based on the Nanohybrids Formed by Chemically Bonding Phosphotungstic Acid with Covalent Organic Frameworks. *J. Power Sources* **2023**, *554*, 232332. [[CrossRef](#)]
34. Han, B.; Song, J.; Liang, S.; Chen, W.; Deng, H.; Ou, X.; Xu, Y.-J.; Lin, Z. Hierarchical NiCo₂O₄ Hollow Nanocages for Photoreduction of Diluted CO₂: Adsorption and Active Sites Engineering. *Appl. Catal. B* **2020**, *260*, 118208. [[CrossRef](#)]
35. Kou, M.; Wang, Y.; Xu, Y.; Ye, L.; Huang, Y.; Jia, B.; Li, H.; Ren, J.; Deng, Y.; Chen, J.; et al. Molecularly Engineered Covalent Organic Frameworks for Hydrogen Peroxide Photosynthesis. *Angew. Chem. Int. Ed. Engl.* **2022**, *61*, e202200413. [[CrossRef](#)] [[PubMed](#)]
36. Zhao, W.; Yan, P.; Li, B.; Bahri, M.; Liu, L.; Zhou, X.; Clowes, R.; Browning, N.D.; Wu, Y.; Ward, J.W.; et al. Accelerated Synthesis and Discovery of Covalent Organic Framework Photocatalysts for Hydrogen Peroxide Production. *J. Am. Chem. Soc.* **2022**, *144*, 9902–9909. [[CrossRef](#)]
37. Li, L.; Xu, L.; Hu, Z.; Yu, J.C. Enhanced Mass Transfer of Oxygen through a Gas–Liquid–Solid Interface for Photocatalytic Hydrogen Peroxide Production. *Adv. Funct. Mater.* **2021**, *31*, 202106120. [[CrossRef](#)]
38. Luo, Y.; Zhang, B.; Liu, C.; Xia, D.; Ou, X.; Cai, Y.; Zhou, Y.; Jiang, J.; Han, B. Sulfone-Modified Covalent Organic Frameworks Enabling Efficient Photocatalytic Hydrogen Peroxide Generation Via One-Step Two-Electron O₂ Reduction. *Angew. Chem. Int. Ed. Engl.* **2023**, *62*, e202305355. [[CrossRef](#)]

39. Chen, W.; Han, B.; Tian, C.; Liu, X.; Liang, S.; Deng, H.; Lin, Z. Mofs-Derived Ultrathin Holey Co₃O₄ Nanosheets for Enhanced Visible Light Co₂ Reduction. *Appl. Catal. B* **2019**, *244*, 996–1003. [[CrossRef](#)]
40. Zhang, Y.; Qiu, J.Y.; Zhu, B.C.; Fedin, M.V.; Cheng, B.; Yu, J.G.; Zhang, L.Y. ZnO/COF S-Scheme Heterojunction for Improved Photocatalytic H₂O₂ Production Performance. *Chem. Eng. J.* **2022**, *444*, 136584. [[CrossRef](#)]
41. Chen, N.; Zhou, Y.; Cao, S.; Wang, R.; Jiao, W. A Novel Strategy for Loading Metal Cocatalysts onto Hollow Nano-TiO₂ Inner Surface with Highly Enhanced H₂ Production Activity. *Green Energy Environ.* **2023**, *8*, 509–518. [[CrossRef](#)]
42. Zhou, S.; Shi, Y.; Chen, G.; Kong, W.; Hu, H.; Xie, H.; Li, C.; Qin, J.; Zhang, Z.; Peng, L.; et al. Fragmentation Engineering on the Edge of Hydroxy-Functional COFs for the Enhanced Photocatalytic Production of H₂O₂ and Direct Photo-Oxidation of Benzene to Phenol in Aqueous Systems. *Chem. Eng. J.* **2023**, *477*, 146946. [[CrossRef](#)]
43. Ma, X.H.; Hou, H.G.; Yang, J.; Liu, J.L.; Liu, G.W.; Du, F.; Qiao, G.J. Porous Si Loaded with Ag Nanoparticles for Ultra-Broadband Infrared Absorption and Detection. *Opt. Mater.* **2023**, *138*, 113651. [[CrossRef](#)]
44. Xu, X.; Sa, R.; Huang, W.; Sui, Y.; Chen, W.; Zhou, G.; Li, X.; Li, Y.; Zhong, H. Conjugated Organic Polymers with Anthraquinone Redox Centers for Efficient Photocatalytic Hydrogen Peroxide Production from Water and Oxygen under Visible Light Irradiation without Any Additives. *ACS Catal.* **2022**, *12*, 12954–12963. [[CrossRef](#)]
45. He, Y.; Zhao, J.; Sham, Y.-T.; Gao, S.; Pan, M.; Chen, Q.; Huang, G.; Wong, P.K.; Bi, J. Efficient Hydrogen Peroxide Photosynthesis over Cds/COF for Water Disinfection: The S-Scheme Pathway, Oxygen Adsorption, and Reactor Design. *ACS Sustain. Chem. Eng.* **2023**, *11*, 17552–17563. [[CrossRef](#)]
46. You, D.; Pan, Z.; Cheng, Q. COFs-Ph@Cds S-Scheme Heterojunctions with Photocatalytic Hydrogen Evolution and Efficient Degradation Properties. *J. Alloys Compd.* **2023**, *930*, 167069. [[CrossRef](#)]
47. Li, Y.; Xu, H.; Ouyang, S.; Lu, D.; Wang, X.; Wang, D.; Ye, J. In Situ Surface Alkalinized G-C₃N₄ toward Enhancement of Photocatalytic H₂ Evolution under Visible-Light Irradiation. *J. Mater. Chem. A* **2016**, *4*, 2943–2950. [[CrossRef](#)]
48. Liu, Y.; Tan, H.; Wei, Y.; Liu, M.; Hong, J.; Gao, W.; Zhao, S.; Zhang, S.; Guo, S. Cu₂O/2D COFs Core/Shell Nanocubes with Antiphotocorrosion Ability for Efficient Photocatalytic Hydrogen Evolution. *ACS Nano* **2023**, *17*, 5994–6001. [[CrossRef](#)]
49. Hao, F.; Yang, C.; Lv, X.; Chen, F.; Wang, S.; Zheng, G.; Han, Q. Photo-Driven Quasi-Topological Transformation Exposing Highly Active Nitrogen Cation Sites for Enhanced Photocatalytic H₂O₂ Production. *Angew. Chem. Int. Ed. Engl.* **2023**, *62*, e202315456. [[CrossRef](#)]
50. Vinogradov, K.Y.; Bulanova, A.V.; Shafigulin, R.V.; Tokranova, E.O.; Mebel, A.M.; Zhu, H. Density Functional Theory Study of the Oxygen Reduction Reaction Mechanism on Graphene Doped with Nitrogen and a Transition Metal. *ACS Omega* **2022**, *7*, 7066–7073. [[CrossRef](#)]
51. Jung, S.; Senthil, R.A.; Min, A.; Kumar, A.; Moon, C.J.; Jeong, G.H.; Kim, T.W.; Choi, M.Y. Exploring Ir-Doped Nife-Ldh Nanosheets Via a Pulsed Laser for Oxygen Evolution Kinetics: In Situ Raman and Dft Insights. *J. Mater. Chem. A* **2024**. [[CrossRef](#)]
52. Li, G.; Fu, P.; Yue, Q.; Ma, F.; Zhao, X.; Dong, S.; Han, X.; Zhou, Y.; Wang, J. Boosting Exciton Dissociation by Regulating Dielectric Constant in Covalent Organic Framework for Photocatalysis. *Chem Catalysis* **2022**, *2*, 1734–1747. [[CrossRef](#)]

Disclaimer/Publisher's Note: The statements, opinions and data contained in all publications are solely those of the individual author(s) and contributor(s) and not of MDPI and/or the editor(s). MDPI and/or the editor(s) disclaim responsibility for any injury to people or property resulting from any ideas, methods, instructions or products referred to in the content.